

See discussions, stats, and author profiles for this publication at: <https://www.researchgate.net/publication/263939526>

Silicon-Based Thermoelectrics Made from a Boron-Doped Silicon Dioxide Nanocomposite

ARTICLE in CHEMISTRY OF MATERIALS · DECEMBER 2013

Impact Factor: 8.35 · DOI: 10.1021/cm401990c

CITATIONS

2

READS

43

13 AUTHORS, INCLUDING:



[Christina Birkel](#)

Technical University Darmstadt

28 PUBLICATIONS 311 CITATIONS

[SEE PROFILE](#)



[Tristan Day](#)

California Institute of Technology

15 PUBLICATIONS 369 CITATIONS

[SEE PROFILE](#)



[Xiulei David Ji](#)

Oregon State University

57 PUBLICATIONS 3,407 CITATIONS

[SEE PROFILE](#)



[Stephan Kraemer](#)

University of California, Santa Barbara

35 PUBLICATIONS 1,026 CITATIONS

[SEE PROFILE](#)

Silicon-Based Thermoelectrics Made from a Boron-Doped Silicon Dioxide Nanocomposite

Matthew L. Snedaker,^{†,‡} Yichi Zhang,^{†,‡} Christina S. Birkel,^{†,‡,§} Heng Wang,[§] Tristan Day,[§] Yifeng Shi,^{||} Xiulei Ji,[⊥] Stephan Kraemer,[#] Carolyn E. Mills,[†] Armin Moosazadeh,[†] Martin Moskovits,[†] G. Jeffrey Snyder,[§] and Galen D. Stucky^{*,†,‡}

[†]Department of Chemistry and Biochemistry, University of California, Santa Barbara, California 93106-9510, United States

[‡]Materials Research Laboratory, University of California, Santa Barbara, California 93106-5121, United States

[§]Materials Science, California Institute of Technology, Pasadena, California 91106, United States

^{||}College of Materials, Chemistry and Chemical Engineering, Hangzhou Normal University, Hangzhou 310036, P. R. China

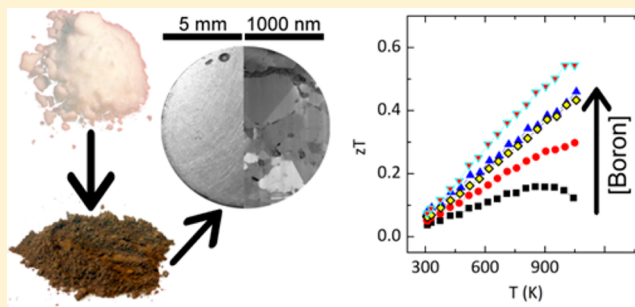
[⊥]Department of Chemistry, Oregon State University, Corvallis, Oregon 97331, United States

[#]Materials Department, University of California, Santa Barbara, California 93106-5050, United States

S Supporting Information

ABSTRACT: We report a method for preparing p-type silicon germanium bulk alloys directly from a boron-doped silica germania nanocomposite. This is the first successful attempt to produce and characterize the thermoelectric properties of SiGe-based thermoelectric materials prepared at temperatures below the alloy's melting point through a magnesiothermic reduction of the silica-germania nanocomposite. We observe a thermoelectric power factor that is competitive with the literature record obtained for high energy ball milled nanocomposites. The large grain size in our hot pressed samples limits the thermoelectric figure of merit to 0.5 at 800 °C for an optimally doped Si₈₀Ge₂₀ alloy.

KEYWORDS: thermoelectrics, silicon germanium, magnesiothermic reduction, silica, germania



INTRODUCTION

The combustion of fossil fuels for power generation is an inefficient process, introducing waste heat into the environment well beyond the energy premium predicted by thermodynamics for an ideal Carnot engine. In the pursuit of energy efficiency, the demand for systems capable of recovering waste heat is increasing. A temperature gradient across a thermoelectric material results in the thermal diffusion of charge carriers from the hot side to the cold side, giving rise to a voltage that can be used to convert waste heat to electricity. The efficiency of this conversion process is judged by the thermoelectric figure of merit, $zT = \alpha^2 \sigma T / (\kappa_L + \kappa_E)$, where T , α , σ , κ_L , and κ_E are the absolute temperature, Seebeck coefficient, electrical conductivity, and the lattice and electronic contributions to the thermal conductivity, respectively. Improving the figure of merit is a significant materials engineering problem due to the interdependence of these properties. Most recent advances in improving thermoelectric efficiency have resulted from nanostructuring the material, which leads to a reduction of the lattice thermal conductivity without significantly decreasing the charge mobility.¹

Silicon germanium alloys (SiGe) are the standard materials used for thermoelectric generators at high temperatures. Two

appealing advantages of these SiGe alloys are that silicon is the second-most earth abundant element and both silicon and germanium are less toxic than other heavy metals commonly used in thermoelectrics. A variety of synthetic strategies have been developed for silicon-based alloys in order to improve the figure of merit and reduce cost.^{2–5} In general, the thermoelectric efficiency of the materials can be improved by increasing nanostructuring to enhance phonon scattering and decrease the thermal conductivity,^{6,7} and the cost is reduced by minimizing the germanium content.^{8,9} High energy ball milling of a mixture of elemental silicon, germanium, and the dopant element in order to decrease the average particle size and the thermal conductivity has been demonstrated to give the highest figure of merit for bulk nanostructured SiGe thermoelectric materials.^{10,11} On the basis of a similar strategy, modulation doping has been further employed as a means to enhance the power factor ($\alpha^2 \sigma$) without significantly increasing the thermal conductivity.^{12,13}

Received: June 19, 2013

Revised: November 20, 2013

However, the ball milled nanocomposites were prepared from relatively costly metallurgical-grade silicon and germanium made through high-temperature ($\sim 2000^\circ\text{C}$) carbothermal reduction of high purity silica and a similar reduction process of germania. Therefore, an alternative strategy to obtain nanostructured SiGe particles directly from nanostructured oxides at low temperature is highly desirable.

Motivated by this goal, several attempts to synthesize hierarchically structured Si and SiC materials from silica at low temperature have been reported.^{14,15} Bao et al. first reported a successful magnesiothermic reduction of silica to silicon at 650°C that maintains the microstructure of the precursor oxide (in their case, a diatom frustule).¹⁶

Although this low temperature route can successfully maintain the microstructure of the precursor oxide since it occurs below silicon's melting point, we are not aware of any studies on the electronic properties of the silicon obtained by this route or application of the magnesiothermic reduction to prepare silicon-based thermoelectrics. Herein, we solve the issues of extrinsic doping and germanium incorporation and describe the first confirmation that the magnesiothermic reduction can be used to produce silicon-based thermoelectric materials and demonstrate that this reaction may offer a low-temperature, cost-effective route to prepare p-type silicon-based thermoelectric materials, with an equivalent power factor ($\sim 20 \mu\text{W cm}^{-1} \text{K}^{-2}$ at 800°C) as the reference alloy (i.e., the one used for NASA's space missions) prepared by the conventional silicon production route.¹¹

In this report, we focus on the doping strategy to tune the carrier density in the $\text{Si}_{1-x}\text{Ge}_x$ alloy by controllably incorporating the dopant into the precursor oxide concurrent with the direct reduction of the precursor silicon and germanium oxides. By creating an optimal carrier density for p-type $\text{Si}_{80}\text{Ge}_{20}$, the best thermoelectric power factor performance obtained using a silica precursor is comparable to the record values reported for the ball-milled material that we will refer to as BM- $\text{Si}_{80}\text{Ge}_{20}$.¹¹ These results suggest a new, potentially cost-effective route for the preparation of $\text{Si}_{1-x}\text{Ge}_x$ alloys that have a high thermoelectric performance. The ability to directly produce nanostructured silicon germanium from nanostructured silica and germania to eliminate time-consuming, high energy ball milling will be presented in a subsequent publication.

■ EXPERIMENTAL SECTION

Synthesis of Silica–Germania Composite and Incorporation of Boron. Tetraethyl orthosilicate (X grams TEOS, 99.999%, Alfa-Aesar) and germanium(IV) ethoxide (Y grams TEOG, 99.995%, Alfa Aesar) were added to a glass vial and bath sonicated for 10 s. This mixture was injected into ethanol (280 mL, 200 proof) that was stirred inside an Erlenmeyer flask by a magnetic stir bar. Aqueous ammonium hydroxide (8.4 mL, 30 wt %, ACS grade, EMD) was added dropwise over 3 min. Then ethanolic boric acid (Z μL of 1 M solution, prepared from Sigma-Aldrich boric acid, 99.99%) was quickly injected, the flask was sealed with parafilm, and the mixture was stirred for 24 h. The parafilm was removed, and the flask was placed in an oven for 24 h at 65°C . The condensate was obtained by vacuum filtration, rinsed with deionized water and ethanol, redispersed in ethanol, and allowed to dry in a crystallization dish at room temperature over several days. The oxide powder was calcined at 500°C for 6 h. In order to obtain $(\text{SiO}_2)_{90}(\text{GeO}_2)_{10}$: $X = 6.768$ and $Y = 0.9126$. In order to obtain $(\text{SiO}_2)_{80}(\text{GeO}_2)_{20}$: $X = 6.016$ and $Y = 1.826$. For the dopant series, $[\text{B}]_1$: $Z = 0$; $[\text{B}]_2$: $Z = 71$; $[\text{B}]_3$: $Z = 710$; and $[\text{B}]_4$: $Z = 7100$.

Magnesiothermic Reduction. A pellet of oxide powder and magnesium powder was prepared by grinding the oxide (0.6 g) with

magnesium (0.6 g, -325 mesh powder, 99.8%, Alfa-Aesar) in acetone with a mortar and pestle until dry. The light gray mixed powder was cold-pressed into a pellet at about 7 tons for ca. 3 min. The pellet was placed inside an open ended quartz tube that was placed at the center of a quartz tube furnace. A 90 sccm argon:10 sccm hydrogen flow was established, and the furnace was heated to 650°C at $4.8^\circ\text{C min}^{-1}$, soaked at 650°C for 6 h, and allowed to cool to room temperature.

Powder Purification. All of the powder contents of the tube were collected into a centrifuge tube and soaked in aqueous hydrochloric acid solution (30 mL, 3 M) for 12 h. The liquid was removed following centrifugation, and the powder was washed again with the hydrochloric acid solution, then agitated by a bath sonicator for 20 min, decanted, washed once more with the hydrochloric acid solution, agitated by a bath sonicator for 20 min, and decanted. Then a hydrofluoric acid solution (~ 30 mL, 3:1 volumetric ratio of 48% aqueous hydrofluoric acid:200 proof ethanol) was poured into the centrifuge tube with the powder. This mixture was sonicated for 20 min, centrifuged, and decanted, and these steps were repeated again. After the second HF solution had been decanted, ethanol (~ 30 mL, 200 proof) was added to the centrifuge tube with powder, sonicated for 20 min, centrifuged, and decanted, and these steps were repeated again. The centrifuge tube with the wetted-powder was placed in a vacuum oven at 50°C for at least 24 h in order to yield a dry, purified powder.

Pelletization and Pellet Processing. About 0.34 g of the SiGe powder was added to a POCO EDM-3 graphite die with an inner diameter of 1.3 cm. The die surfaces that contacted the powder were previously coated with a boron nitride diffusion barrier. The powder was hot-pressed into a pellet at 1200°C and 70 MPa for 2 h. The pellet was removed from the die, and the surface boron nitride was removed from the pellet by sanding with silicon carbide sand paper. The surface of the pellet was further polished with diamond lapping films down to at least $1 \mu\text{m}$ diamond grain size (MultiPrep, Allied High Tech, Inc.). A $\sim 1 \text{ mm} \times 2 \text{ mm} \times 10 \text{ mm}$ bar was cut from the pellet with a low-speed saw fitted with a diamond wafering blade (Allied High Tech Products, Inc.).

XRD Characterization. High resolution synchrotron powder diffraction data were collected at beamline 11-BM at the Advanced Photon Source (APS), Argonne National Laboratory, using a wavelength of $\lambda = 0.41315 \text{ \AA}$. Le Bail fits were performed with TOPAS Academic v4.1.¹⁷

Secondary Ion Mass Spectrometry. A Physical Electronics 6650 Dynamic Secondary Ion Mass Spectrometry (SIMS) system was used to measure the boron to background silicon ratio. A relative sensitivity factor of $4.5 \times 10^{20} \text{ Si cm}^{-3}$, which was obtained for boron-doped, single-crystal silicon, was used to estimate the boron density in the samples.

Microscopy Characterization. Field-emission scanning electron microscopy was performed on a FEI XL40 Sirion FEG microscope with an Oxford Inca X-ray system attached for energy dispersive X-ray spectroscopy. Secondary electron images were collected with an acceleration voltage of 5 kV, and EDX measurements were collected with an acceleration voltage of 20 kV. An electron-transparent lamella of a sample was prepared by low-angle milling with a FEI Focused Ion Beam Helios 600 Dual Beam with Omniprobe. Transmission electron microscopy images were obtained with an FEI T20 electron microscope at an accelerating voltage of 200 kV. TEM EDX measurements were performed with the use of a double-tilt sample holder.

Electronic and Thermal Transport Characterization. The Seebeck coefficient and electrical conductivity in the temperature region between 35 and 800°C were measured simultaneously on bar-shaped samples using a ULVAC ZEM-3 M8. Thermal diffusivity was measured on pellets or half-pellets using a Netzsch laser flash apparatus (LFA 457) in the temperature region between 35 and 800°C , and samples were coated with a thin layer of graphite to minimize errors in the emissivity. The Hall coefficients were measured by the van der Pauw method on a home-built system with 2 T field.

RESULTS AND DISCUSSION

Synthesis of the Silica–Germania Nanocomposite. A silica–germania nanocomposite was synthesized via an adaptation of the modified Stöber method used by Strandwitz et al.^{18,19} Silica germania nanospheres were formed by the ammonia-catalyzed hydrolysis and condensation of a mixture of tetraethyl orthosilicate (TEOS) and germanium(IV) ethoxide (TEOG) dissolved in ethanol. The ratio of silicon to germanium was tuned by adjusting the molar ratio of the TEOS and TEOG precursors.

Boron was incorporated into the oxide by injecting an aliquot of ethanolic boric acid into the precursor solution immediately after the ammonia was added. The volume of the boric acid aliquot was selected based on the boron content desired in the silicon germanium alloy (see Experimental Section). Boron was chosen because (1) it is a common p-type dopant in silicon semiconductors,²⁰ (2) there has been extensive research and development of borosilicates, including borosilicate nanoparticles,²¹ and (3) the incorporation of boron into mesoporous silica SBA-15 has been demonstrated.²² The added boric acid resulting in the desired boron doping concentrations did not affect the particle shape or size for our samples.

Fusion of the oxide nanospheres was achieved through a mild thermal treatment of the oxide condensate and precursor solution before the oxide was isolated by vacuum filtration, rinsed with water and ethanol, redispersed in ethanol, and dried at room temperature. The oxide was then calcined. Figure 1a

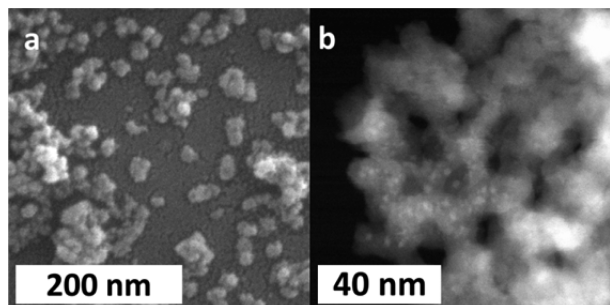
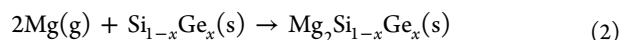
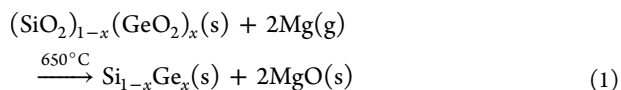


Figure 1. (a) SEM image and (b) STEM image of the calcined $(\text{SiO}_2)_{90}(\text{GeO}_2)_{10}$ composite, which indicates the presence of germania particles (~ 3 nm diameter) embedded in the silica nanoparticle matrix.

presents a scanning electron microscope (SEM) image of the calcined $(\text{SiO}_2)_{90}(\text{GeO}_2)_{10}$ nanocomposite that was obtained, which shows that the particles are monodisperse with an average diameter of ~ 16 nm. Imaging with a scanning transmission electron microscope (STEM) reveals a more complex nanostructure, with ~ 3 nm diameter germania clusters randomly dispersed throughout the oxide matrix (Figure 1b). The electron micrographs indicate that the particles had fused.

Magnesiothermic Reduction, Powder Purification, and Pelletization. The oxide was mixed with magnesium powder and pressed into a pellet, which was placed in the center of a tube furnace. The magnesiothermic reduction was performed at 650°C for 6 h under an argon–hydrogen gas flow. The reduction follows the chemical equations:



with overreaction of the SiGe product with magnesium producing silicide–germanides. After the reduction, all of the powder is collected from the tube (most of the particles in the collected powder appear as shown in Supporting Information Figure S1). The magnesia, excess magnesium, silicide, and germanide phases are selectively etched with aqueous hydrochloric acid (see XRD pattern in Supporting Information Figure S2). The unreacted silica and germania are then selectively etched with a hydrofluoric acid solution. The silicon–germanium is rinsed with ethanol and then dried in a vacuum oven to yield a brown powder (Figure 2a, inset).

High-resolution synchrotron powder X-ray diffraction data (Figure 2a) for the clean, dry $\text{Si}_{90}\text{Ge}_{10}$ powder indicate separate phases of germanium and silicon, with Le Bail fits giving an average germanium grain size of 8.5 nm and an average silicon grain size of approximately 200 nm. This phase segregation is in agreement with an observation made by Szczech et al.²³

The average silicon grain size of 200 nm is about 15 times larger than the grain size obtained by groups that performed the reduction on silicon dioxide nanostructures;^{16,24} however, this may be attributed to the oxide being in intimate contact with the magnesium powder (instead of the reduction relying upon Mg–vapor transport), the longer reduction time that we have used, and/or efficient crystal nucleation around the germanium nanoparticles, which form before the silicon dioxide starts to reduce. Since germanium dioxide can be reduced to germanium with hydrogen gas at temperatures below magnesium's melting point,²⁵ the germanium nanoparticles may act as seeds for the silicon crystallization. SEM images of the clean, dry $\text{Si}_{90}\text{Ge}_{10}$ powder show that germanium dots decorate the surface of the porous matrix (Figure 2c).

The XRD data also indicate the presence of a trace silicon carbide (SiC) impurity phase, which was significantly lessened when the oxides were calcined before the magnesiothermic reduction. The SiGe powder is consolidated into a pellet (Figure 2b inset) by hot pressing at 1200°C and 70 MPa for 2 h, which causes the germanium nanodots to alloy into the silicon matrix, as shown by the disappearance of the Ge reflections in the XRD pattern for the $\text{Si}_{90}\text{Ge}_{10}$ pellet (Figure 2b). The average $\text{Si}_{90}\text{Ge}_{10}$ grain size calculated from the single-phase Le Bail fit is 500 nm. The germanium is considered to completely alloy into the silicon because the Ge(111) reflection disappears and the lattice constant of $5.44448(1)$ Å calculated on the basis of the SiGe(111) diffraction peak is in agreement with the lattice constant measured for the $\text{Si}_{90}\text{Ge}_{10}$ alloy.²⁶

After polishing the pellet (shown in the inset of Figure 2b) with diamond lapping films, SEM images of the sample's surface (Figure 2d) were obtained. The surface is characterized by regions rich in silicon germanium (darker) and lighter regions that are rich in magnesium and fluorine, as determined by energy dispersive X-ray spectroscopy with a lateral resolution of ~ 50 nm (EDX).

A lamella was obtained from a $\text{Si}_{90}\text{Ge}_{10}$ pellet by focused ion beam etching in order to investigate the grain sizes and grain interfaces by transmission electron microscopy. The inset of Supporting Information Figure S3a shows a TEM image of the lamella prepared from a $\text{Si}_{90}\text{Ge}_{10}$ pellet. The sample is composed of grains that range in size from tens of nanometers up to a micrometer. The large grains are silicon germanium. EDX measurements suggest that the silicon germanium composition is spatially homogeneous in the large grains.

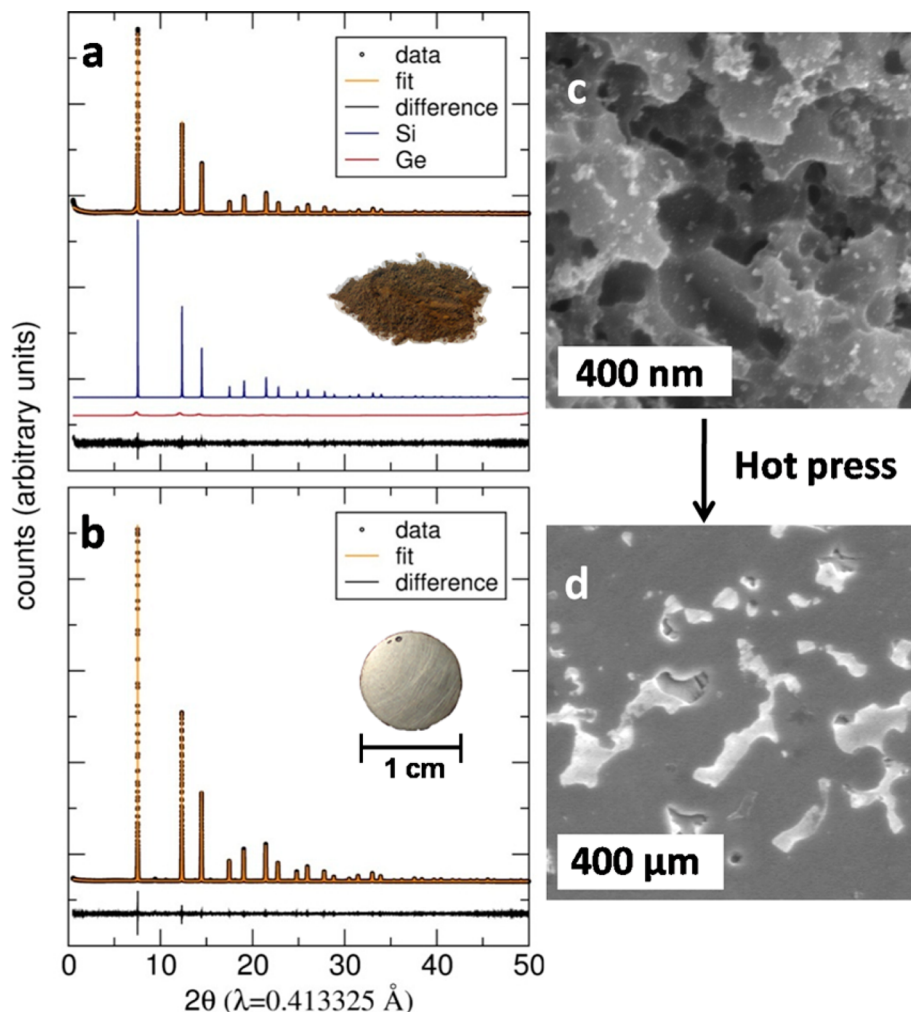


Figure 2. (a) Synchrotron X-ray powder diffraction data (black circles), two-phase Le Bail fit (orange line) corresponding to the segregated silicon (blue line) and germanium (red line) phases, and difference profile (black line) of the reduced, purified $\text{Si}_{90}\text{Ge}_{10}$ powder. (b) Synchrotron X-ray powder diffraction data (black circles) and single-phase Le Bail fit (orange line) corresponding to the $\text{Si}_{90}\text{Ge}_{10}$ alloy and difference profile (black line) of the annealed $\text{Si}_{90}\text{Ge}_{10}$ compound. An SEM image of the reduced, purified $\text{Si}_{90}\text{Ge}_{10}$ powder appears in (c) and an SEM image of the pressed, polished $\text{Si}_{90}\text{Ge}_{10}$ pellet appears in (d).

Table 1. Summary of the Compositional and Carrier Properties of the Samples Discussed in This Paper^a

sample	EDX Si:Ge	EDX Mg [atom % Mg]	density [g cm^{-3}] ^b	SIMS B density [B cm^{-3}]	hole density [cm^{-3}]	hole mobility [$\text{cm}^2 \text{V}^{-1} \text{s}^{-1}$]
$\text{Si}_{90}\text{Ge}_{10}\text{---}[\text{B}]_1$	89:11	5.0	2.58 (96.2%)	1.25×10^{19}	1.42×10^{19}	31
$\text{Si}_{90}\text{Ge}_{10}\text{---}[\text{B}]_2$	92:8	3.8	2.54 (94.7%)	5.09×10^{19}	5.18×10^{19}	29
$\text{Si}_{90}\text{Ge}_{10}\text{---}[\text{B}]_3$	92:8	3.3	2.58 (96.2%)	4.39×10^{20}	1.35×10^{20}	29
$\text{Si}_{90}\text{Ge}_{10}\text{---}[\text{B}]_4$	91:9	3.7	2.63 (98.0%)	1.52×10^{21}	1.44×10^{20}	27
$\text{Si}_{80}\text{Ge}_{20}\text{---}[\text{B}]_3$	82:18	1.1	2.97 (98.8%)	2.32×10^{20}	1.55×10^{20}	28

^aThe relative standard deviations are <5% for SIMS B density, ~1% for the hole density, and ~1% for hole mobility, respectively. ^bThe mass-density column includes the density relative to the theoretical density for the nominal Si:Ge composition.²⁶

Supporting Information Figure S3b shows the SiGe(111) lattice planes in the large grain marked “1” (Supporting Information Figure S3).

Some of the boundaries of the SiGe grains (such as region “2” which is shown magnified in Supporting Information Figure S3c) interface with an impurity phase that is rich in magnesium and fluorine, as determined by EDX. The TEM analysis also indicates that the SiC impurity phase that was observed by XRD is due to SiC nano-inclusions that are embedded in the SiGe grains. Supporting Information Figure S3d shows a high

resolution TEM image (HR-TEM) of an embedded SiC nanoparticle from region “3”.

The mass densities of the pellet samples were determined by the Archimedeian method. The measured densities are greater than 94% of the corresponding alloy’s density. The Si:Ge ratio and the atomic percentage of magnesium were characterized by EDX measurements on several regions across the samples’ surfaces. The densities and atomic compositions data for the samples discussed in this paper are provided in Table 1. The densities of the samples are all high enough such that their

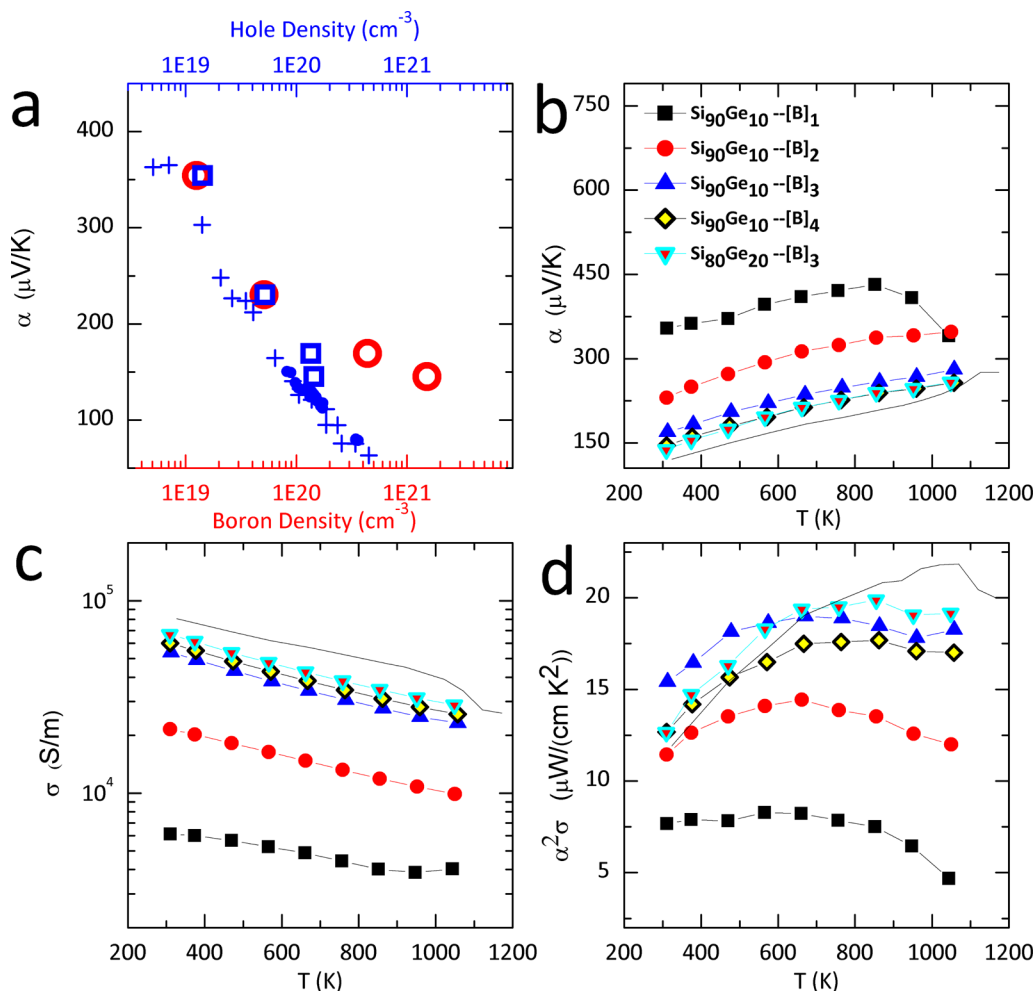


Figure 3. (a) Dependence of room-temperature Seebeck coefficient on the boron density (red ring) and the hole density (blue box) for the $\text{Si}_{90}\text{Ge}_{10}-[\text{B}]_i$ doping series, including the data reported for p-type $\text{Si}_{70}\text{Ge}_{30}$ (blue crosses)³⁰ and p-type $\text{Si}_{80}\text{Ge}_{20}$ (blue circles).²⁸ Temperature dependence of the (b) Seebeck coefficient, (c) electrical conductivity, and (d) power factor for bulk-nanostructured $\text{Si}_{1-x}\text{Ge}_x$ alloys of varying boron content. The boron content increases from $[\text{B}]_1$ to $[\text{B}]_4$. The solid trace represents the data from BM- $\text{Si}_{80}\text{Ge}_{20}$.¹¹

effective thermoelectric properties are representative of their host thermoelectric properties (see Supporting Information).

Secondary ion mass spectrometry (SIMS) was applied to estimate the boron content in our samples, with the boron signal referenced to the silicon signal and a relative sensitivity factor of $4.5 \times 10^{20} \text{ Si cm}^{-3}$, which was measured for a single crystal of boron-doped silicon. The effectiveness of our doping strategy is shown in Table 1 and in the SIMS depth profile (Supporting Information Figure S4), where we have demonstrated reproducibility and the ability to control the boron content over 2 orders of magnitude. We detect a significant amount of boron in the unintentionally doped $\text{Si}_{90}\text{Ge}_{10}-[\text{B}]_1$, which we attribute to boron contamination from the glassware used during the oxide synthesis.

Thermoelectric Characterization. As the thermoelectric properties of a material are strongly dependent upon the carrier density, we used our doping strategy to prepare a doping series for the $\text{Si}_{90}\text{Ge}_{10}$ composition ($\text{Si}_{90}\text{Ge}_{10}-[\text{B}]_i$). The hole density and mobility in the samples were measured by the van der Pauw method.²⁷ The boron incorporation strategy we have developed is observed to be an effective means of tuning the carrier density, as seen in Table 1, where the hole density increases with the boron density measured by SIMS. We achieved an optimal hole density in the $\text{Si}_{90}\text{Ge}_{10}$ composition,

which is also close to the previously determined optimal level ($\sim 1.5 \times 10^{20} \text{ cm}^{-3}$) for $\text{Si}_{80}\text{Ge}_{20}$.²⁸

With a knowledge of the boron content that produces an optimal carrier density in a $\text{Si}_{90}\text{Ge}_{10}$ alloy and because the optimal carrier density does not vary significantly with the alloy composition,²⁹ we prepared a $\text{Si}_{80}\text{Ge}_{20}$ sample with a near-optimal carrier density so that we could compare the thermoelectric properties of the material prepared by our magnesiothermic reduction route to a $\text{Si}_{80}\text{Ge}_{20}$ nanocomposite prepared by the ball-milling route.¹¹

The electrical conductivity and Seebeck coefficient were measured from room temperature to 800 °C on a $\sim 1 \text{ mm} \times 2 \text{ mm} \times 10 \text{ mm}$ bar that was diced from each pellet with a low-speed saw fitted with a diamond wafering blade. The room temperature Seebeck coefficients for the $\text{Si}_{90}\text{Ge}_{10}-[\text{B}]_i$ doping series are plotted as a function of carrier density and boron density in Figure 3a, showing that the Seebeck coefficient decreases with increasing carrier density. Our results for this doping series agree well with previously reported carrier density dependent Seebeck coefficient measurements on p-type $\text{Si}_{80}\text{Ge}_{20}$ and p-type $\text{Si}_{70}\text{Ge}_{30}$.^{28,30} The discrepancy between hole density and boron density for the two highest doped samples is likely due to boron precipitation, which limits the number of electrically active boron atoms and, thus, the hole

density. The hole density in the highest doped sample (i.e., $\text{Si}_{90}\text{Ge}_{10}\text{---}[\text{B}]_4$) is an order of magnitude lower than the boron density.

Up to 800 K, the Seebeck coefficients for the $\text{Si}_{90}\text{Ge}_{10}\text{---}[\text{B}]_i$ series and the optimally doped $\text{Si}_{80}\text{Ge}_{20}$ alloy (Figure 3b) increase with increasing temperature, with the exception of the $\text{Si}_{90}\text{Ge}_{10}\text{---}[\text{B}]_1$ sample, where a maximum of the Seebeck coefficient was observed around 800 °C due to the contribution from minority carriers in lightly doped samples.

The electrical conductivities of the $\text{Si}_{90}\text{Ge}_{10}\text{---}[\text{B}]_i$ doping series and the optimally doped $\text{Si}_{80}\text{Ge}_{20}$ alloy are presented in Figure 3c. With increasing boron content in the $\text{Si}_{90}\text{Ge}_{10}\text{---}[\text{B}]_i$ doping series, we observed increasing electrical conductivity. The electrical conductivity for the optimally doped $\text{Si}_{90}\text{Ge}_{10}$ is comparable to that of the optimally doped $\text{Si}_{80}\text{Ge}_{20}$. The electrical conductivity of all of the samples decreases as a function of temperature, which is expected for degenerately doped semiconductors. The optimally doped $\text{Si}_{90}\text{Ge}_{10}\text{---}[\text{B}]_3$ exhibits an approximately 80% increase in power factor at 1000 K compared to the unintentionally doped $\text{Si}_{90}\text{Ge}_{10}\text{---}[\text{B}]_1$ (Figure 3d). Our high-temperature power factor for the optimally doped $\text{Si}_{80}\text{Ge}_{20}\text{---}[\text{B}]_3$ alloy is $\sim 20 \mu\text{W cm}^{-1} \text{K}^{-2}$ in the temperature range from 700 to 1000 K, approximately 10% lower than that reported for BM- $\text{Si}_{80}\text{Ge}_{20}$.¹¹

The thermal diffusivities of the $\text{Si}_{1-x}\text{Ge}_x$ alloys were measured by the laser flash method from room temperature to 800 °C. The thermal conductivity was determined from the product of the temperature-dependent thermal diffusivity, the room temperature mass density, and the temperature dependent heat capacity measured by Amano et al. for the $\text{Si}_{80}\text{Ge}_{20}$ composition (for the $\text{Si}_{90}\text{Ge}_{10}$ composition, the heat capacity was estimated using the Dulong-Petit value, which slightly underestimates the heat capacity).³¹ For the carrier density range explored in the $\text{Si}_{90}\text{Ge}_{10}\text{---}[\text{B}]_i$ doping series, the $[\text{B}]_1$ sample is the only one to exhibit a bipolar contribution to the thermal conductivity at temperatures greater than 900 K (Figure 4a). However, the thermal conductivities of the $[\text{B}]_2$, $[\text{B}]_3$, and $[\text{B}]_4$ $\text{Si}_{90}\text{Ge}_{10}$ alloys do not increase in the order of increasing electrical conductivity as one would expect from the Wiedemann–Franz law. This trend may be due to differences in microstructure (including porosity and impurity content) or electron–phonon scattering with increasing carrier density, which occurs in this degenerate-doping regime.³² The $\text{Si}_{80}\text{Ge}_{20}\text{---}[\text{B}]_3$ alloy is expected to have a lower thermal conductivity than the $\text{Si}_{90}\text{Ge}_{10}$ samples; however, the thermal conductivity of the $\text{Si}_{90}\text{Ge}_{10}$ samples is estimated using the heat capacity from the Dulong-Petit value, which underestimates the heat capacity and hence the thermal conductivity.

The thermal conductivity of our optimally doped $\text{Si}_{80}\text{Ge}_{20}$ alloy at 800 °C is approximately 10% lower than the thermal conductivity reported for a non-nanostructured, optimally doped p-type $\text{Si}_{80}\text{Ge}_{20}$ radioisotope thermoelectric generator (RTG) used for space missions.^{11,28} However, compared to BM- $\text{Si}_{80}\text{Ge}_{20}$, the grain sizes in the samples reported here are almost 30 times larger, which leads to our $\text{Si}_{80}\text{Ge}_{20}$ alloy having a thermal conductivity at 800 °C that is about 50% higher than the ball-milled and hot-pressed nanocomposite. The larger grain sizes are due to the synthetic conditions we have employed and the dramatic grain growth during the consolidation process (2 h at 1200 °C and 70 MPa). The grain size may be minimized by using vapor transport for the magnesiothermic reduction and by using a more rapid consolidation process such as spark plasma sintering or rapid

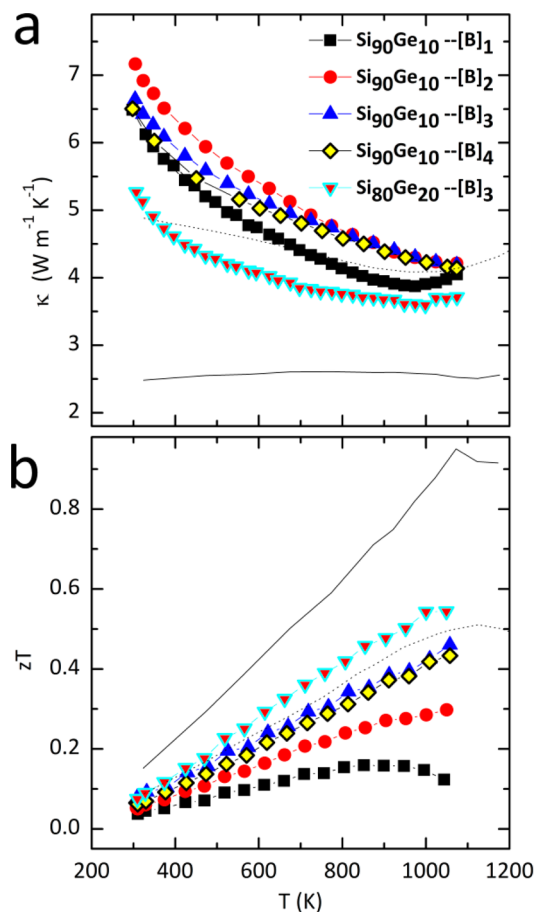


Figure 4. Temperature dependence of the (a) thermal conductivity and (b) thermoelectric figure of merit for $\text{Si}_{1-x}\text{Ge}_x$ alloys of varying boron content prepared by magnesiothermic reduction of a silica germania nanocomposite. The thermal conductivity is calculated from thermal diffusivity, Archimedeian density, and relevant heat capacity (i.e., the literature-reported, temperature-dependent heat capacity of $\text{Si}_{80}\text{Ge}_{20}$ or the Dulong-Petit value for $\text{Si}_{90}\text{Ge}_{10}$). The dotted trace represents the data for RTG- $\text{Si}_{80}\text{Ge}_{20}$, and the solid trace represents the data for BM- $\text{Si}_{80}\text{Ge}_{20}$.¹¹

hot pressing.³³ The ability to directly produce nanostructured silicon from nanostructured silica and germania by the magnesiothermic reduction approach will be presented in more detail in a subsequent publication.

The zT values of the $\text{Si}_{1-x}\text{Ge}_x$ alloy that we prepared via magnesiothermic reduction of a boron-doped silica germania nanocomposite are shown as a function of temperature in Figure 4b. The optimally doped $\text{Si}_{80}\text{Ge}_{20}$ alloy has a zT of 0.5 (800 °C). The maximum zT for our $\text{Si}_{80}\text{Ge}_{20}$ alloy is in agreement with the RTG material (0.5 at 800 °C) but about 40% lower than the zT (800 °C) of 1 for the nanostructured bulk BM- $\text{Si}_{80}\text{Ge}_{20}$ alloy, as a result of the larger grain size in our alloy.^{11,28} The maximum power factor of our optimally doped $\text{Si}_{80}\text{Ge}_{20}$ alloy is in agreement with the RTG material ($\sim 20 \mu\text{W cm}^{-1} \text{K}^{-2}$ at 800 °C).

CONCLUSIONS

In summary, p-type $\text{Si}_{1-x}\text{Ge}_x$ alloys prepared by hot-pressing the product from a magnesiothermic reduction of a boron-doped silica germania nanocomposite have been shown to have comparable thermoelectric properties to p-type $\text{Si}_{1-x}\text{Ge}_x$ alloys prepared by the conventional carbothermal reduction route.

The carrier density and electronic properties were tuned by varying the boron content in the precursor oxide, which resulted in a power factor that is competitive with the record values in compositionally homogeneous p-type Si₈₀Ge₂₀ nanocomposites. The large grain size in our alloys results in a relatively high thermal conductivity, which is currently the limiting factor in the thermoelectric efficiency of our alloys. We expect the figure of merit to be further enhanced by minimizing the grain growth during the magnesiothermic reduction and consolidation process. These studies are in progress.

■ ASSOCIATED CONTENT

■ Supporting Information

XRD patterns of the material during the different processing steps, TEM images, compositional properties, carrier properties, and SIMS depth profiles for the samples. This material is available free of charge via the Internet at <http://pubs.acs.org>.

■ AUTHOR INFORMATION

Corresponding Author

*E-mail: (G.D.S.) stucky@chem.ucsb.edu.

Author Contributions

[#]The manuscript was written through contributions of all authors. All authors have given approval to the final version of the manuscript.

Author Contributions

[#]These authors contributed equally (M.L.S., Y.Z., C.S.B.).

Notes

The authors declare no competing financial interest.

■ ACKNOWLEDGMENTS

This work was supported by the Center for Energy Efficient Materials, an Energy Frontier Research Center, funded by the U.S. D.O.E., Office of Basic Energy Science, under Award No. DE-SC0001009. The MRL Central Facilities are supported by the MRSEC Program of the NSF under Award Nos. DMR05-20415 and DMR11-21053, a member of the NSF-funded Materials Research Facilities Network. C.S.B. is a recipient of the Feodor Lynen Research Fellowship supported by the Alexander von Humboldt foundation. Y.Z. is a recipient of the Corning Fellowship, supported by the Corning Science Foundation. Use of the Advanced Photon Source at Argonne National Laboratory was supported by the U.S. Department of Energy, Office of Science, Office of Basic Energy Sciences, under Contract No. DE-AC02-06CH11357. H.W., T.D., and G.J.S. thank NASA/JPL for support. Y.S. thanks NSFC (21103038) for support. We would like to thank Ben Curtin, Peter Burke, Dr. Thomas E. Mates, and Deryck Stave for their valuable insight and contributions.

■ REFERENCES

- (1) Snyder, G. J.; Toberer, E. S. *Nat. Mater.* **2008**, *7*, 105–114.
- (2) Minnich, A. J.; Dresselhaus, M. S.; Ren, Z. F.; Chen, G. *Energy Environ. Sci.* **2009**, *2*, 466–479.
- (3) Bux, S. K.; Rodriguez, M.; Yeung, M. T.; Yang, C.; Makhluaf, A.; Blair, R. G.; Fleurial, J.-P.; Kaner, R. B. *Chem. Mater.* **2010**, *22*, 2534–2540.
- (4) Ikeda, T.; Haviez, L.; Li, Y.; Snyder, G. J. *Small* **2012**, *8*, 2350–2355.
- (5) Yi, T.; Chen, S.; Li, S.; Yang, H.; Bux, S.; Bian, Z.; Katcho, N. A.; Shakouri, A.; Mingo, N.; Fleurial, J.-P.; Browning, N. D.; Kauzlarich, S. M. *J. Mater. Chem.* **2012**, *22*, 24805–24813.
- (6) Dresselhaus, M. S.; Chen, G.; Tang, M. Y.; Yang, R. G.; Lee, H.; Wang, D. Z.; Ren, Z. F.; Fleurial, J.-P.; Gogna, P. *Adv. Mater.* **2007**, *19*, 1043–1053.
- (7) Rowe, D. M.; Shukla, V. S.; Savvides, M. *Nature* **1981**, *290*, 765–766.
- (8) Zhu, G. H.; Lee, H.; Lan, Y. C.; Wang, X. W.; Joshi, G.; Wang, D. Z.; Yang, J.; Vashaee, D.; Guilbert, H.; Pillitteri, A.; Dresselhaus, M. S.; Chen, G.; Ren, Z. F. *Phys. Rev. Lett.* **2009**, *102*, 196803.
- (9) Bux, S. K.; Blair, R. G.; Gogna, P. K.; Lee, H.; Chen, G.; Dresselhaus, M. S.; Kaner, R. B.; Fleurial, J.-P. *Adv. Funct. Mater.* **2009**, *19*, 2445–2452.
- (10) Wang, X. W.; Lee, H.; Lan, Y. C.; Zhu, G. H.; Joshi, G.; Wang, D. Z.; Yang, J.; Muto, A. J.; Tang, M. Y.; Klatsky, J.; Song, S.; Dresselhaus, M. S.; Chen, G.; Ren, Z. F. *Appl. Phys. Lett.* **2008**, *93*, 193121.
- (11) Joshi, G.; Lee, H.; Lan, Y.; Wang, X.; Zhu, G.; Wang, D.; Gould, R. W.; Cuff, D. C.; Tang, M. Y.; Dresselhaus, M. S.; Chen, G.; Ren, Z. F. *Nano Lett.* **2008**, *8*, 4670–4674.
- (12) Zebarjadi, M.; Joshi, G.; Zhu, G.; Yu, B.; Minnich, A.; Lan, Y.; Wang, X.; Dresselhaus, M. S.; Ren, Z. F.; Chen, G. *Nano Lett.* **2011**, *11*, 2225–2230.
- (13) Yu, B.; Zebarjadi, M.; Wang, H.; Lukas, K.; Wang, H.; Wang, D.; Opeil, C.; Dresselhaus, M. S.; Chen, G.; Ren, Z. F. *Nano Lett.* **2012**, *12*, 2077–2082.
- (14) Shi, Y.; Zhang, F.; Hu, Y. S.; Sun, X.; Zhang, Y.; Lee, H. I.; Chen, L.; Stucky, G. D. *J. Am. Chem. Soc.* **2010**, *132*, 5552–5553.
- (15) Fang, J.; Kang, C. B.; Huang, Y.; Tolbert, S. H.; Pilon, L. *J. Phys. Chem. C* **2012**, *116*, 12926–12933.
- (16) Bao, Z.; Weatherspoon, M. R.; Shian, S.; Cai, Y.; Graham, P. D.; Allan, S. M.; Ahmad, G.; Dickerson, M. B.; Church, B. C.; Kang, Z.; Abernathy, H. W., III; Summers, C. J.; Liu, M.; Sandhage, K. H. *Nature* **2007**, *446*, 172–175.
- (17) Coelho, A. *TOPAS Academic*, Version 4.1; Coelho Software: Brisbane, Australia, 2007.
- (18) Stöber, W.; Fink, A. *J. Colloid Interface Sci.* **1968**, *26*, 62–69.
- (19) Strandwitz, N. C.; Stucky, G. D. *Chem. Mater.* **2009**, *21*, 4577–4582.
- (20) Sze, S. M.; Irvin, J. C. *Solid-State Electron.* **1968**, *11*, 599–602.
- (21) Parashar, V. K.; Orhan, J. B.; Sayah, A.; Cantoni, M.; Gijs, M. A. M. *Nat. Nanotechnol.* **2008**, *3*, 589–594.
- (22) van Grieken, R.; Escola, J. M.; Moreno, J.; Rodriguez, R. *Chem. Eng. J.* **2009**, *155*, 442–450.
- (23) Szczec, J. R.; Lukowski, M. A.; Jin, S. *J. Mater. Chem.* **2010**, *20*, 8389–8393.
- (24) Richman, E. K.; Kang, C. B.; Brezesinski, T.; Tolbert, S. H. *Nano Lett.* **2008**, *8*, 3075–3079.
- (25) Dennis, L. M.; Tressler, K. M.; Hance, F. E. *J. Am. Ceram. Soc.* **1923**, *45*, 2033–2047.
- (26) Dismukes, J. -P.; Ekstrom, L.; Paff, R. J. *J. Phys. Chem.* **1964**, *68*, 3021–3027.
- (27) van der Pauw, L. J. *Philips Res. Rep.* **1958**, *13*, 1–9.
- (28) Vining, C. B.; Laskow, W.; Hanson, J. O.; Van der Beck, R. R.; Gorsuch, P. D. *J. Appl. Phys.* **1991**, *69*, 4333–4340.
- (29) Minnich, A. J.; Lee, H.; Wang, X. W.; Joshi, G.; Dresselhaus, M. S.; Ren, Z. F.; Chen, G.; Vashaee, D. *Phys. Rev. B* **2009**, *80*, 155327.
- (30) Slack, G. A.; Hussain, M. A. *J. Appl. Phys.* **1991**, *70*, 2694–2718.
- (31) Amano, T.; Beaudry, B. J.; Gschneidner, K. A.; Hartman, R.; Vining, C. B.; Alexander, C. A. *J. Appl. Phys.* **1987**, *62*, 819–823.
- (32) Steigmeier, E. F.; Abeles, B. *Phys. Rev.* **1964**, *136*, A1149–A1155.
- (33) LaLonde, A. D.; Ikeda, T.; Snyder, G. J. *Rev. Sci. Instrum.* **2011**, *82*, 025104.